Bulletin of the Seismological Society of America, Vol. 100, No. 3, pp. 910–922, June 2010, doi: 10.1785/0120080250

Trade-Offs among Dynamic Parameters Inferred from Results of Dynamic Source Inversion

by Hiroyuki Goto and Sumio Sawada

Abstract Dynamic rupture simulations have been performed in order to generate a physically consistent slip distribution. In these simulations, an attempt has been made to investigate the governing parameters, called dynamic parameters, of historical earthquakes. However, it has been reported that the parameters are not estimated accurately when only the ground motion records are employed; this is because of the trade-offs existing between the parameters, for example, between the strength excess and the slip-weakening distance. In this article, we apply a dynamic source inversion to 2D synthetic tests in order to discuss parameter trade-offs. Sensitivity tests, which consist of numerous sets of inversions including a fixed stage and a released stage, are conducted such that a particular set of estimation parameters is not estimated in the fixed stage; then all of the parameters are estimated in the released stage. The results imply trade-offs between the rupture time and other parameters. From detailed comparisons between slip rates and waveforms, it is observed that the shapes of the slip-rate profiles between the rupture time and the peak time do not contribute well to the generated waveforms. From a simple 1D assumption, a gradient of the slip-weakening friction law, namely, a weakening gradient, is analytically related to the peak-to-rupture time with a -1 slope in the log–log plot. The values estimated from the synthetic tests almost mirror the values of the -1 slope. The results imply the trade-offs between the weakening gradient and the peak-to-rupture time.

Introduction

Dynamic rupture simulations can generate a physically consistent slip distribution based on tectonic loadings, fault geometries, frictions, material properties, and other physical quantities. Simulation models of historical earthquakes have been investigated in order to understand the physical aspects of the earthquakes (e.g., Miyatake, 1992b; Bouchon, 1997; Aochi and Fukuyama, 2002; Harris *et al.* 2002; Dalguer *et al.*, 2002, 2003; Song and Beroza, 2004; Zhang *et al.*, 2004; Miyatake *et al.*, 2004; Aagaard *et al.*, 2004; and Fukuyama and Mikumo, 2006).

In source modeling, the governing parameters are mainly divided into stress parameters and frictional parameters. A stress-time history, estimated from the slip distribution inferred from the results of the kinematic source inversion method, has been discussed with respect to the former parameters. Quin (1990) obtained a distribution of the dynamic stress drop that matches with the kinematic results obtained by trial and error for the 1979 Imperial Valley earthquake. Further, Miyatake (1992a) determined the static stress drop by solving the elastic equilibrium equation through the application of a slip distribution estimated from kinematic results; they calculated the dynamic stress drop at 80% of the static stress drop. They also discussed the peak stress determined from the stress values at the rupture front. In addition, Bouchon (1997) proposed a technique for calculating stress-time histories from a kinematic slip distribution and discussed the stress parameters of four major events.

For frictional parameters, Ide and Takeo (1997) estimated a constitutive relationship from the slip displacements based on the equation of motion. They found that the resolution of small slip-weakening distances was worse in deep parts of a fault. Further, for estimating the slip-weakening distance, Pulido and Irikura (2000) proposed an estimation method that considers the temporal change in the apparent stress. In addition, Mikumo *et al.* (2003) focused on the correlation between the peak time of the slip rate and the time of the slip displacement that corresponds to the slip-weakening distance. Moreover, scaling of dynamic parameters from small (laboratory) to large (earthquake) has also provided some information from experimental and theoretical points of view (e.g., Ohnaka, 2003).

Recently, dynamic parameters are being directly estimated by comparing the observed waveforms of ground motions with the synthetic waveforms calculated from the dynamic parameters. An inversion method, which is based on waveform comparison, is the dynamic source inversion

method. Peyrat and Olsen (2004) applied a neighborhood algorithm for estimating the initial stress distribution of the 2000 Tottori earthquake. Goto and Sawada (2006a, 2006b) theoretically selected a set of independent variables from dynamic parameters and proposed an inversion algorithm that excludes dependent variables. However, it has been pointed out that the waveforms generated by a particular set of dynamic parameters are indistinguishable from those generated by another set of parameters because of parameter trade-offs, for example, between the strength excess and the slip-weakening distance (Guatteri and Spudich, 2000), and between the initial stress and the yield traction or the slip-weakening distance (Peyrat *et al.*, 2004, Corish *et al.*, 2007).

Estimated dynamic parameters might comprise one set of possible solutions detected from the data on bandlimited waveforms. Therefore, understanding the trade-offs among the dynamic parameters evaluated from observed waveforms is very important when developing dynamic source inversions.

In this article, we focus on the trade-offs among the dynamic parameters inferred from the results of dynamic source inversion. Two-dimensional synthetic tests are adopted to efficiently perform a number of simulations. In addition, sensitivity tests are applied in order to detect the parameter trade-offs. Subsequently, the accurately estimated results are selected in order to quantitatively clarify the trade-offs.

Dynamic Source Inversion Method

We summarize the dynamic source inversion method presented by Goto and Sawada (2006a, 2006b). In this article, a 2D *SH* field is selected in order to calculate the rupture propagations that are numerically simulated by solving two governing equations, namely, a friction law and a representation of the traction change. Further, the external stress field is assumed to be constant during the seismic rupture propagation.

Let S be a single planar fault embedded in a 2D *SH* half-space V (Fig. 1). x_1 and x_2 are the axes of a Cartesian system and are aligned parallel and perpendicular to fault S, respectively. This article discusses the slip displacements produced by antiplane shear $\Delta u(x_1, t)$ occurring at time t, which propagates in the x_1 direction. It develops perpendicular to the plane formed by x_1 and x_2.

A number of friction laws have been proposed by various researchers. One of the simplest is the slip-weakening friction law proposed by Ida (1972). Despite its simplicity, it appears to provide a reasonable representation of the basic behavior of a fault rupture. Day *et al.* (2005) formulated the following friction law by combining the associated flow rule and softening (weakening):

$$\begin{aligned} &T_c(x_1) - T(x_1, t) \geq 0, \\ &[T_c(x_1) - T(x_1, t)]\Delta\dot{u}(x_1, t) = 0, \end{aligned} \tag{1}$$

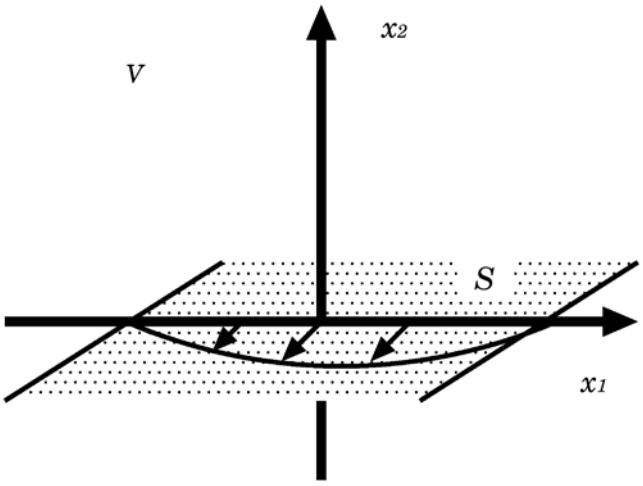

Figure 1. Planar fault S embedded in 2D *SH* half-space V.

$$T_c(x_1) = \begin{cases} -\frac{T_p(x_1) - T_r(x_1)}{D_C(x_1)} \times \Delta u(x_1, t) + T_p(x_1) \\ \quad \text{for } \Delta u(x_1, t) < D_C(x_1) \\ T_r(x_1) \\ \quad \text{for } D_C(x_1) \leq \Delta u(x_1, t), \end{cases} \tag{2}$$

where T denotes the traction; T_c, the yield surface represented by the traction; T_p, the initial value of the yield surface, which is called the yield traction; T_r, the residual traction; and D_C, the slip-weakening distance. The conventional representations of equations (1) and (2) are normalized by the normal stress. However, we use the tractions explicitly because the following numerical calculations do not consider the changes in the normal stress.

A boundary integral equation (BIE) for a full-space field is applied in order to define a representation of the traction change from the initial traction. The explicit BIE for the 2D *SH* field derived by Cochard and Madariaga (1994) is

$$\begin{aligned} T(x_1, t) = T_I(x_1) &- \frac{\mu}{2\beta}\Delta\dot{u}(x_1, t) \\ &- \frac{\mu}{2\pi}\int_S d\xi \int_0^t \frac{\partial\Delta\dot{u}(\xi, \tau)}{\partial\xi} \frac{\sqrt{(t-\tau)^2 - r^2/\beta^2}}{(t-\tau)(x-\xi)} \\ &\times H(t - \tau - r/\beta)d\tau, \end{aligned} \tag{3}$$

where $H(t)$ represents the Heaviside step function; ξ, the point on the fault where a unit load is applied; τ, the time at which the unit load is applied; μ, the shear modulus; β, the S-wave velocity; r, the distance defined by $|x_1 - \xi|$; and T_I, the initial traction.

In the numerical simulation, equations (1), (2), and (3) are discretized. Let the slip-rate $\Delta\dot{u}(x_1, t)$ be represented as

$$\Delta\dot{u}(x_1,t) = \sum_{n=1}^{\infty}\sum_{l=1}^{Nx}\Delta\dot{u}^{ln}\cdot\phi_l(x_1)\cdot\psi_n(t) = \sum_{n=1}^{\infty}\sum_{l=1}^{Nx}\Delta\dot{u}^{ln}\cdot\phi_0[x_1-(l-1)\Delta x]\cdot\psi_0[t-(n-1)\Delta t], \quad (4)$$

where ϕ_0 denotes a prescribed space function; ψ_0, a prescribed time function; Δx, the unit space shift; and Δt, the unit time shift. Nx denotes the number dividing the fault S. If ψ_0 satisfies the causality condition ($\psi_0(t \le 0) = 0$), equation (4) becomes a bounded summation. Here, we choose the following simple boxcar functions for the prescribed functions:

$$\phi_0(x_1) = H(x_1+\Delta x/2) - H(x_1-\Delta x/2), \quad (5)$$

$$\psi_0(t) = H(t) - H(t-\Delta t). \quad (6)$$

The friction law and the BIE are discretized as

$$T_c^l - T^{ln} \ge 0, \qquad [T_c^l - T^{ln}]\Delta\dot{u}^{ln} = 0, \quad (7)$$

$$T_c^l = \begin{cases} -\frac{T_p^l - T_r^l}{D_C^l}\cdot\Delta u^{ln} + T_p^l & \text{for } \Delta u^{ln} < D_C^l \\ T_r^l & \text{for } D_C^l \le \Delta u^{ln}, \end{cases} \quad (8)$$

$$T^{ln} = T_I^l - \frac{\mu}{2\beta}\Delta\dot{u}^{ln} + \sum_{j=1}^{Nx}\sum_{k=1}^{n-1}B^{jkln}\Delta\dot{u}^{jk}, \quad (9)$$

where Δu^{ln} is defined as

$$\Delta u^{ln} \equiv \Delta u^{ln-1} + \Delta t\cdot\Delta\dot{u}^{ln}. \quad (10)$$

Here, T^{ln} denotes the traction at $x_1 = (l-1/2)\Delta x$ and $t = n\Delta t$. B^{jkln} represents the integrated kernel. The simulation method that employs the discretized BIE (equation 9) is known as the boundary integral equation method (BIEM).

At each instant, the fault plane is divided into two regions, namely, a slipping region and a locked region. In the slipping region, the generated traction is constrained on the yield surface, namely, $T_C^l = T^{ln}$. Further, the discretized friction law (equation 8) and the discretized BIE (equation 9) are consolidated into the following two equations:

$$T_p^l = T_I^l - \frac{\mu}{2\beta}\Delta\dot{u}^{ln} + \sum_{j=1}^{Nx}\sum_{k=1}^{n-1}B^{jkln}\Delta\dot{u}^{jk} + (T_p^l - T_r^l)\cdot\frac{\Delta u^{ln}}{D_C^l} \quad \text{for } \Delta u^{ln} < D_C^l, \quad (11)$$

$$T_r^l = T_I^l - \frac{\mu}{2\beta}\Delta\dot{u}^{ln} + \sum_{j=1}^{Nx}\sum_{k=1}^{n-1}B^{jkln}\Delta\dot{u}^{jk} \quad \text{for } D_C^l \le \Delta u^{ln}. \quad (12)$$

Equations (11) and (12) are converted into explicit representations of the slip displacement at $t = n\Delta t$.

$$\Delta u^{ln} = f_a^l\cdot F^{ln} + f_b^l \quad \text{for } \Delta u^{ln} < D_C^l, \quad (13)$$

$$\Delta u^{ln} = F^{ln} + f_c^l \quad \text{for } D_C^l \le \Delta u^{ln}, \quad (14)$$

where

$$F^{ln} = \Delta u^{ln-1} + \frac{2\beta}{\mu}\sum_{j=1}^{Nx}\sum_{k=1}^{n-1}B^{jkln}(\Delta u^{jk} - \Delta u^{jk-1}), \quad (15)$$

$$f_a^l = \frac{\mu}{2\beta\Delta t}\Big/\left(\frac{\mu}{2\beta\Delta t} - \frac{T_B^l}{D_C^l}\right), \quad f_b^l = (T_0^l - T_B^l)\Big/\left(\frac{\mu}{2\beta\Delta t} - \frac{T_B^l}{D_C^l}\right), \quad f_c^l = \frac{2\beta\Delta t}{\mu}\cdot T_0^l. \quad (16)$$

In equation (16), T_B and T_0 are defined as $T_B \equiv T_p - T_r$ and $T_0 \equiv T_I - T_r$, respectively. T_B represents the breakdown stress drop; T_0, the static stress drop. The parameters f_a, f_b, and f_c are the variables that depend only on space and not on time. F is calculated from the convolution of the kernels and the slip time histories until $t = (n-1)\Delta t$.

In the locked region, the slip displacements are usually represented as follows:

$$\Delta u^{ln} = 0 \quad \text{for } T^{ln} < T_p^l. \quad (17)$$

Goto and Sawada (2006a) pointed out the undesirable sensitivity at the rupture start if the rupture start is controlled by T_p, when the inversion of T_p is performed. The slip displacement starts to develop when the generated traction is equal to T_p. However, when T_p is estimated, the searching range may not have been determined before the estimations because the upper bound of the generated traction are not given. When T_p is set to be larger than the upper bound for an element, the element becomes a barrier to the rupture. Then, slip is not generated at the element. In contrast, when T_p is set to be smaller than the upper bound, the element can rupture. These two behaviors abruptly change between certain values of the yield traction. Thus, the generated slips abruptly disappear when the searched T_p value exceeds the upper peak of the traction.

Goto and Sawada suggested an alternative concept, that is, to introduce the rupture start time t_r as a criterion of the rupture start instead of using T_p as the criterion. The searching range of t_r does not have an upper limit; it does not de-

pend on the upper peaks of the generated tractions. This concept specifies the rupture time of each element; the rupture time seems to be different from that obtained using general spontaneous rupture simulation, which gives the distribution of the strength excess and generates the distribution of the rupture time. However, inversion analysis is a procedure for modeling the dynamic rupture that has already been given. We only make an attempt to find the distribution of the strength excess or the rupture time in order to explain the given dynamic rupture model. Furthermore, neither the strength excess nor the rupture time can be given any priority if they are associated with each other.

From the definition of t_r, T_0 can be represented by a function of t_r and T_B because the slip displacement satisfies both equations (13) and (17) at $t_r = n_r \Delta t$

$$T_0^l = -\frac{\mu}{2\beta \Delta t} \cdot F^{ln_r} + T_B^l. \tag{18}$$

Equations (13) and (14) are recursively applied to calculate the slip displacement Δu for every time step when D_C, T_B, and t_r are specified for the fault. Therefore, our objective is to estimate the control parameters D_C, T_B, and t_r.

The generated slips cause a seismic wave in the surrounding medium. The synthetic seismic waves are represented by a convolution of slips and the first space derivatives of Green's function. In the dynamic source inversion method, the misfit between the synthetic and observed waveforms is minimized. In order to assess the misfit, the following nonlinear objective function is applied:

$$J = \sum_{ns} \frac{\|\boldsymbol{u}^{ns*} - \boldsymbol{u}^{ns}(\boldsymbol{x})\|^2}{\|\boldsymbol{u}^{ns*}\| \|\boldsymbol{u}^{ns}(\boldsymbol{x})\|} \rightarrow \min, \tag{19}$$

where $\boldsymbol{u}^*$ and $\boldsymbol{u}$ denote the vectors of the observed and synthetic waveforms at each site ns, respectively; $\boldsymbol{x}$ indicates a vector of the space distribution of the estimation parameters. The equation (19) definition of J is different from that given by Goto and Sawada (2006a). This is because the original definition of J does not constrain the results preferring to be no rupture propagations. For example, the J value obtained from the original definition becomes constant when the estimated parameters do not generate a rupture. In such a case, the parameters constitute the local minimum solution. In order to avoid such a situation, we apply the alternative definition of J in which J increases when the generated waveforms are quite small.

Multiscale Inversion Technique

For the inversion analysis, Goto and Sawada (2006b) applied a multiscale technique by introducing the Walsh function. $\varphi_k(x)$ is a multistep function whose value is 1 or -1 defined in $x = (0, 1)$ (Walsh, 1923). Let a_i be a discrete function ($i = 0, \cdots, N-1$), where N denotes the number of discretizations of the fault length L. a_i can be expressed as a series of Walsh functions, $\varphi_k(x)$, as follows:

$$a_i = \sum_{k=0}^{N-1} \hat{a}_k \cdot \varphi_k\left(\frac{i}{N}\right), \tag{20}$$

where $\hat{a}_k$ indicates the coefficient of the kth-order Walsh function $\varphi_k(x)$, placed in sequence according to the Walsh order. The zero-order Walsh function, $\varphi_0(x)$, is a constant ($= 1$). Assume that the scale length of a Walsh function equals the minimum length of the continuous values of 1 or -1; that is, let the scale lengths of φ_0, φ_1, and φ_2 be L, $L/2$, and $L/4$, respectively. The relation between the scale length ls and the order k is

$$ls^m = \frac{L}{2^m} \quad \text{for } 2^{m-1} \le k < 2^m. \tag{21}$$

If N can be expressed as an integral power of 2, the summation in equation (20) can be separated by a series of summations with the same scale lengths,

$$a_i = \hat{a}_0 \cdot \varphi_0\left(\frac{i}{N}\right) + \hat{a}_1 \cdot \varphi_1\left(\frac{i}{N}\right) + \sum_{k=2}^{2^2-1} \hat{a}_k \cdot \varphi_k\left(\frac{i}{N}\right) + \cdots + \sum_{k=N/2}^{N-1} \hat{a}_k \cdot \varphi_k\left(\frac{i}{N}\right), \tag{22}$$

and the mth scale approximation is defined as follows:

$$\bar{a}_i^m \equiv \hat{a}_0 \cdot \varphi_0\left(\frac{i}{N}\right) + \cdots + \sum_{k=2^{m-1}}^{2^m-1} \hat{a}_k \cdot \varphi_k\left(\frac{i}{N}\right). \tag{23}$$

Thus, the mth scale approximation does not have a scale length smaller than ls. In the multiscale inversion analysis, the dynamic parameters are represented by equation (23). Further, a steep change in the dynamic parameters connecting the constant parts of a Walsh function is not directly related to the generation of a high-frequency component, because a continuous slip distribution is guaranteed on the basis of the equation of motion. For a 2D fault, a series of Walsh functions is applied to two mutually perpendicular directions; the representation becomes a double summation of the series similar to a 2D Fourier series.

The multiscale inversion technique estimates the parameters from a low scale to a high scale. Figure 2 shows a schematic diagram of this technique. The initial parameters are set at $\bar{a}_i^0$, and by using the conjugate gradient method, a suitable coefficient $\hat{a}_0$ is estimated by solving the optimum problem defined by equation (19). Then the estimated results are applied recursively to the initial parameters in the next higher scale. A different low-pass filter is applied for the observed waveforms in each scale because the detectable scale length of an estimation parameter corresponds to the frequency range of the observed waveforms. Goto and Sawada (2006b) defined the threshold frequency f^m as being related to the scale length according to the following relationship:

$$f^m = \frac{\beta}{ls^m}. \tag{24}$$

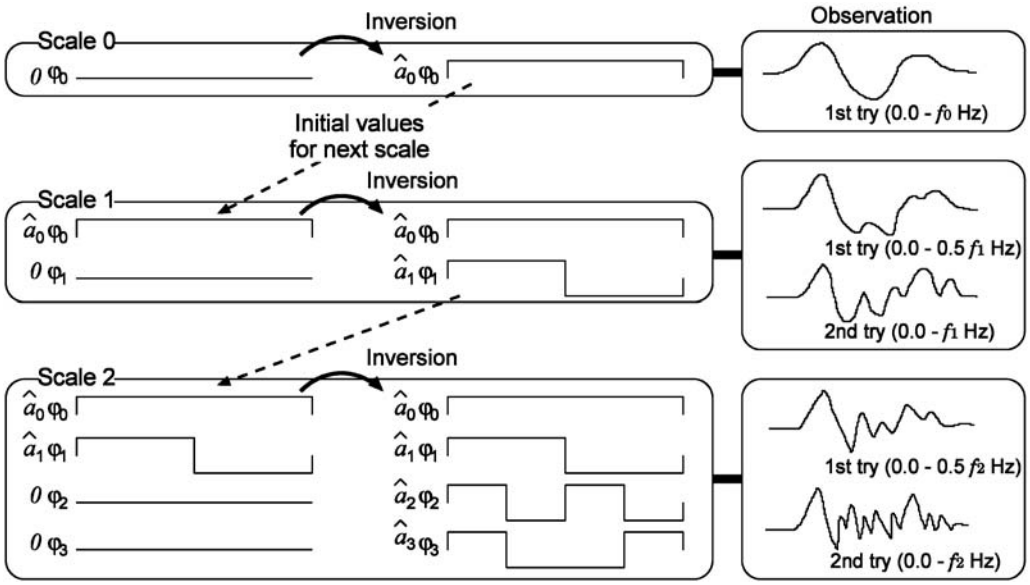

Figure 2. Schematic diagram of the multiscale inversion technique. Additional inversion steps with an intermediate frequency range are introduced in order to avoid a jump in the threshold frequency.

However, a jump in the threshold frequency between scales may interrupt the seamless evaluation of the estimated parameters. One method to avoid such a jump is to introduce additional inversion steps with an intermediate frequency range that is half of the threshold frequency, as shown in Figure 2.

Models

A planar fault, whose length is 12 km, top depth is 3 km, and dip angle is 80°, is embedded in a 2D *SH* half-space with a density ρ of 3100 kg/m^3 and *S*-wave velocity β of 3820 m/sec (Fig. 3). The space element Δx is set at 93.75 m, which is independent of the scales of the inversion analysis, and has a time interval of $\Delta t = 0.01$ sec. Further, no contributions of the free surface to the rupture propagation are assumed because the fault does not come in contact with the free surface and the high fault dip of 80° is assumed (e.g., Goto *et al.*, 2008). Synthetic waveforms are compared at 10 observation sites located at 2 km intervals along the free surface. The waveforms are the convolution of the slip time histories and theoretical Green's functions for the homogeneous half-space. In the inversion analysis, the distributions of dynamic parameters on the fault are estimated on the basis of the synthetic waveforms at the 10 sites.

Three distributions of the dynamic parameters, namely, models A, B, and C, are assumed in order to calculate the synthetic waveforms (Fig. 4). All models that are located at a distance of 6375–7500 m from the fault top have a nucleation zone length of 1125 m. In each zone, the static stress drop, T_0, is 11.0 MPa, and the breakdown stress drop, T_B, is 10.0 MPa. Model A and B both have a single high-stress-drop region and a single region with a short slip-weakening distance: In model A, the former and latter regions are located in the fault-width ranges of 6000–9000 m and 3000–9000 m, respectively; in model B, both the regions are located in the fault-width range of 3000–6000 m. Model C has the same distributions of the breakdown stress drop and the slip-weakening distance as model A, while the rupture velocity is set to be constant with 80% of the *S*-wave velocity by controlling the static stress drop. If the generated slip displacement is shorter than the modeled slip-weakening distance, the final slip displacement is regarded as the slip-weakening distance, and the related traction change is regarded as the breakdown stress drop. Consequently, the

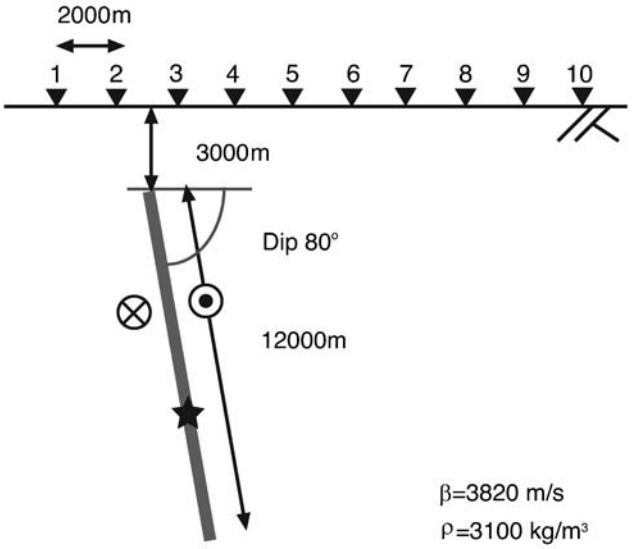

Figure 3. Model of the 2D synthetic tests. A planar fault (length: 12 km, top depth: 3 km, and dip angle: 80°) is embedded in a 2D *SH* half-space. Ten observation sites are located at 2-km intervals along the free surface.

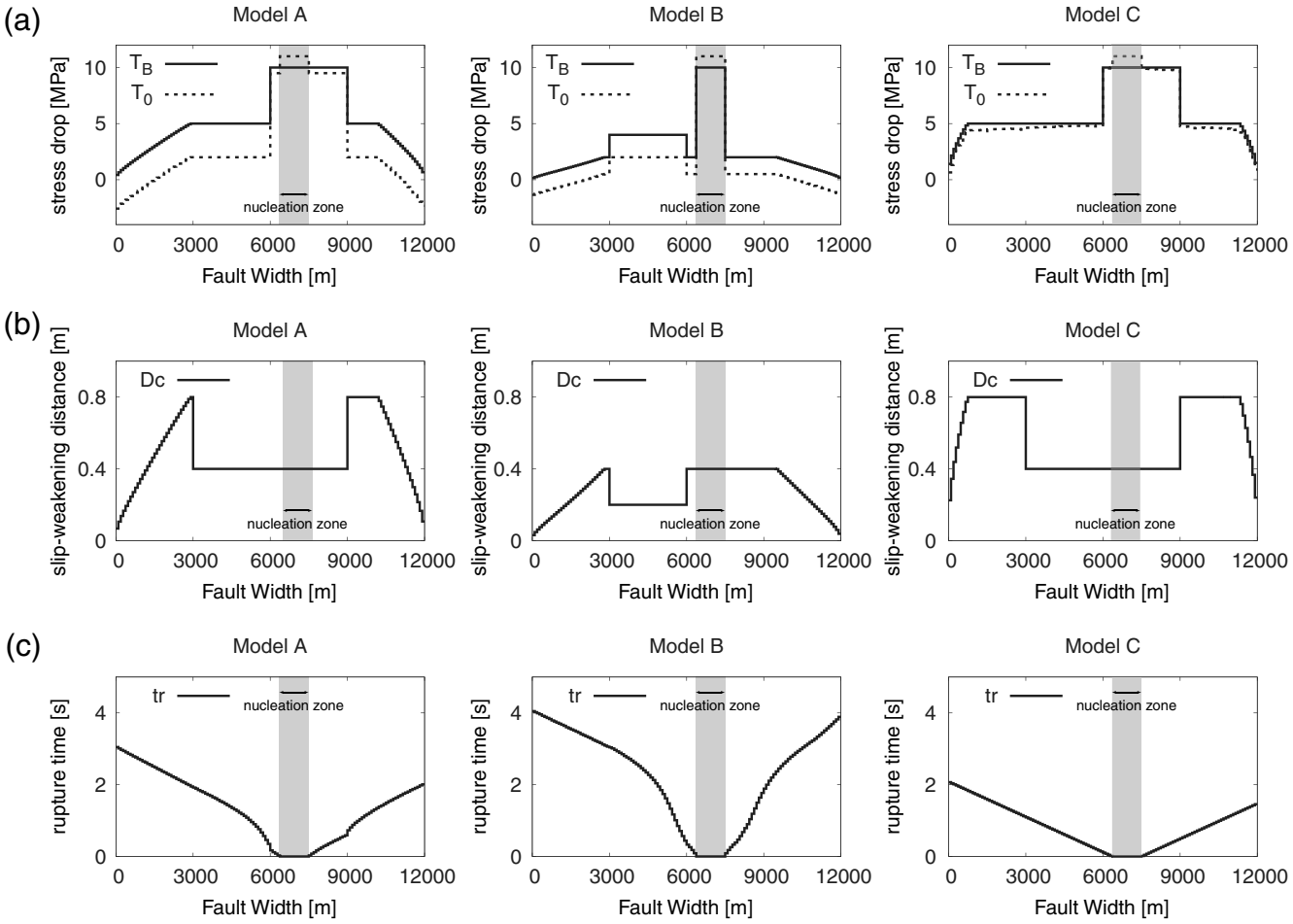

Figure 4. Three distributions (model A on the left, model B in the center, and model C on the right) of the dynamic parameters, namely, the breakdown stress drop, static stress drop, slip-weakening distance, and rupture time.

distributions of slip-weakening distances and stress drops beside the fault edges are reduced, as shown in Figure 4a, b. The average rupture velocities are about 2000 m/sec for model A and 1500 m/sec for model B. For model C, the rupture velocity is constant at 3056 m/sec. The generated rupture propagation for model B is slower than that for models A and C.

Numerical Tests and Discussions

In general, the trade-offs among estimation parameters are discussed for nonlinear optimization problems. For dynamic source models, several researchers have discussed the trade-offs that must be made among dynamic parameters in order to represent synthetic waveforms. Guatteri and Spudich (2000) pointed out a trade-off between the strength excess ($T_p - T_I$) and the slip-weakening distance (D_C) by modeling a hypothetical event of the 1979 Imperial Valley earthquake. They discussed the possibility of stably estimating the fracture energy. Peyrat *et al.* (2004) estimated the dynamic rupture process for the 1992 Landers earthquake. They assumed one asperity model and two barrier models. For the asperity model, which had a constant yield traction and slip-weakening distance, the distribution of the initial traction was estimated. For the barrier models, which have a constant initial stress, either the yield traction or the slip-weakening distance was estimated. All of the three models are estimated models. They are generated from synthetic data that agree well with the observed strong ground motion records, InSAR and the GPS data. It was concluded that the observed data could not indicate which model was adequate. Corish *et al.* (2007) performed synthetic tests on the nonlinear rupture inversion method for a hypothetical event of the 2000 western Tottori earthquake. They estimated the distributions of the initial traction and the slip-weakening distance, while the yield traction and the residual traction were assumed to be constant. In their results, a positive linear correlation was found between the mean initial traction and the slip-weakening distance.

A multiscale inversion analysis is carried out from the zero scale to the second scale, and it is found that the resolution of the analysis is 3 km after the second scale. The estimation parameters are D_C, T_B, and the rupture velocity distribution v_r instead of t_r. v_r is considered instead of t_r because the rupture time distribution is generally not constant.

In contrast, when the rupture velocity distribution is represented by the zero scale approximation of its Walsh series, it is equivalent to the representation in which the rupture time is proportional to the distance from the hypocenter. Therefore, we regard the rupture velocity as the rupture time in the following discussions. For each scale, the conjugate gradient method is applied to obtain the optimum solution of equation (19). The initial values are set to be $D_C = 0.2$ m and $T_B = 4.0$ MPa. Three cases of rupture velocity $v_r = 0.9\beta$ (Case-vr90), 0.7β (Case-vr70) and 0.5β (Case-vr50) are tested. This implies that three different inversions of the same data are conducted. In addition, a comparison is made between the observed and synthetic velocity waveforms.

Numerical tests are performed in order to investigate the trade-offs among the dynamic parameters by applying sensitivity tests. The tests consist of two stages, namely, the fixed and the released stages, as described next (Fig. 5). The particular set of estimation parameters selected is not identified in the fixed stage. These parameters are not estimated in the fixed stage, while the other parameters are estimated. All the parameters, including the selected parameters, are evaluated in the released stage. For every scale, the tests are performed with fixed and released stages.

If a particular parameter set includes the set of trade-off parameters, the generated waveforms become almost identical. Therefore, when the trade-off parameters are estimated from the waveforms by using the parameter set, there are many local minima in the objective function J. In such a problem, the probability of reaching the local minimum of J increases, and the iteration number of the conjugate gradient method decreases. Then the use of a large number of iterations indicates that J becomes a less local minimum function, and the parameter set does not include the set of trade-off parameters. Basically, all the three dynamic parameters should be estimated because they are mathematically independent. However, when the fixed stages are omitted, the estimated parameters immediately reach the minimum solution, as discussed later. Therefore, the local minimum is reduced by introducing the fixed stage, and the suitable values are searched in the solution space. Then, in the released stage, the local minimum is searched around the estimated values in the fixed stage.

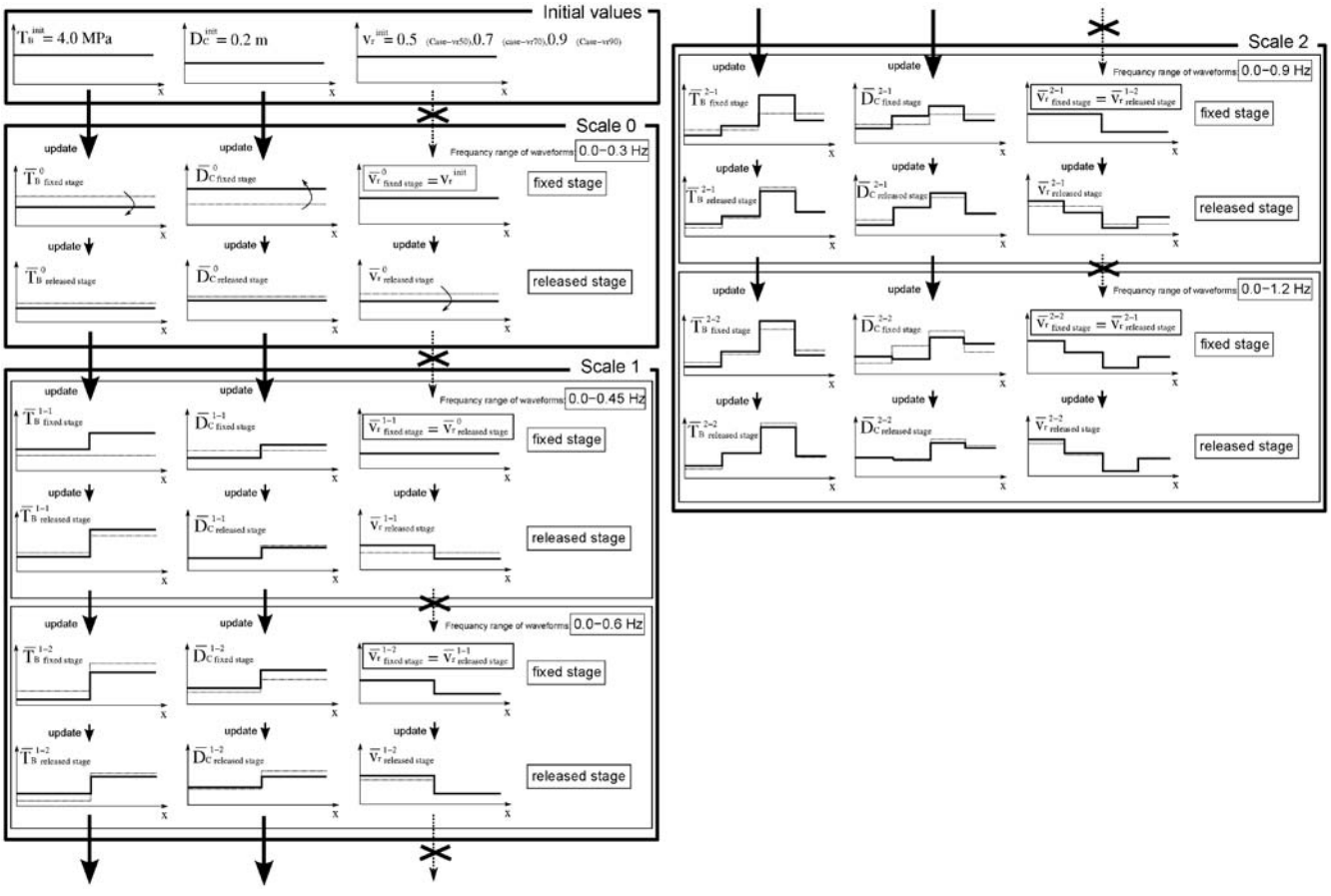

Figure 5. Schematic diagram of the sensitivity tests including the fixed stage and the released stage. It illustrates one of the cases wherein the rupture velocity is a fixed parameter ($[v_r]$). The particular set of estimation parameters selected is not identified in the fixed stage. These parameters are not estimated in the fixed stage, while the other parameters are estimated. In the released stage, all the parameters including the selected parameters are evaluated.

Some pairs of parameters among the dynamic parameters may have a trade-off relationship. If the selected parameters include one of the pairs, the other pairs are more variable in the estimation process. In order to find a trade-off pair, we will examine how variable a parameter is; that is, we will conduct a sensitivity test. Figure 6 (for Case-vr50) and Figure 7 (for Case-vr90) show the convergence histories for the breakdown stress drop, the slip-weakening distance, and the rupture time, which are represented by a root mean square (rms) between the target distributions and the estimated distributions normalized by the target distributions. The total number of iterations is counted through the applied multiscale steps. The number of iterations can be regarded as an index of the difficulty in reaching a local minimum, because iterations continue until the difference between the previous and present values becomes quite small. Here, we define [ ] as the notation for a set of fixed parameters. In these figures, the cases $[v_r]$, $[D_C]$, and $[T_B]$ are compared. No fix indicates the results of a conventional inversion without the fixed stage. If we did not introduce the released stage, it would have been meaningless to discuss the rupture time in the case $[v_r]$ by Figures 6 and 7. However, in this article, the parameter values are modified in the released stage. For example, the rms value of $[v_r]$ for the rupture time (Fig. 6c) is almost constant through the fixed and released stages. From the definition of the fixed stage, the rms value must be constant in the fixed stage, while the values are not well updated during the released stage. Thus, the lines represent the behavior in the released stages.

For models A, B, and C, a larger number of iterations were required for the case of $[v_r]$ than for the other cases. Cases $[D_C]$ and $[T_B]$ require a similar number of iterations as those required by the no fix case. For example, in Figure 6a of model A, which shows the relation between the rms value for the estimated dynamic stress drop and the number of iterations, the number of iterations related to $[v_r]$ is four times larger than those related to the other cases. A rapid decrease in the rms value implies a good performance by the inversion method. For Case-vr50 (Fig. 6), the rms value for the $[v_r]$ of model A decreases with the progression of iterations, while that for $[v_r]$ of model B increases. This may be because for model B, the initial rupture velocity is almost similar to the target velocity (Fig. 4). For Case-vr90 (Fig. 7), a decrease in the rms value for the $[v_r]$ cases of model A and model B is observed for the breakdown stress drop and the slip-weakening distance, while a constant rms value is observed for the rupture time.

According to the sensitivity test results, the rupture parameter (that is, the rupture velocity or the rupture time) has different characteristics from those of the other parameters. This implies that either the slip-weakening distance or the breakdown stress drop has a trade-off relationship with the rupture parameter. If the initial values of the rupture velocity are close to the target values, the rms value for every

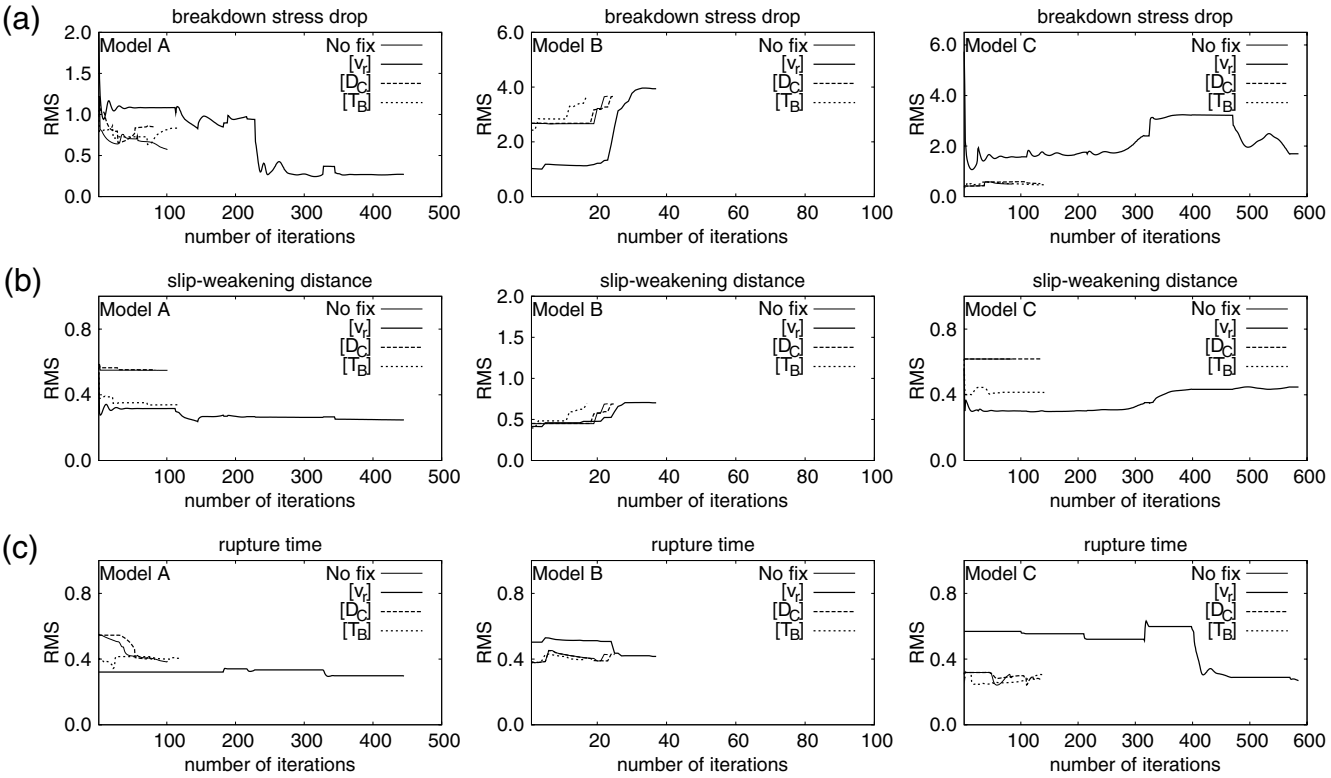

Figure 6. Convergence histories of (a) the breakdown stress drop, (b) the slip-weakening distance, and (c) the rupture time are represented by the rms value for Case-vr50 (model A on the left, model B in the center, and model C on the right). [ ] indicates a set of fixed parameters.

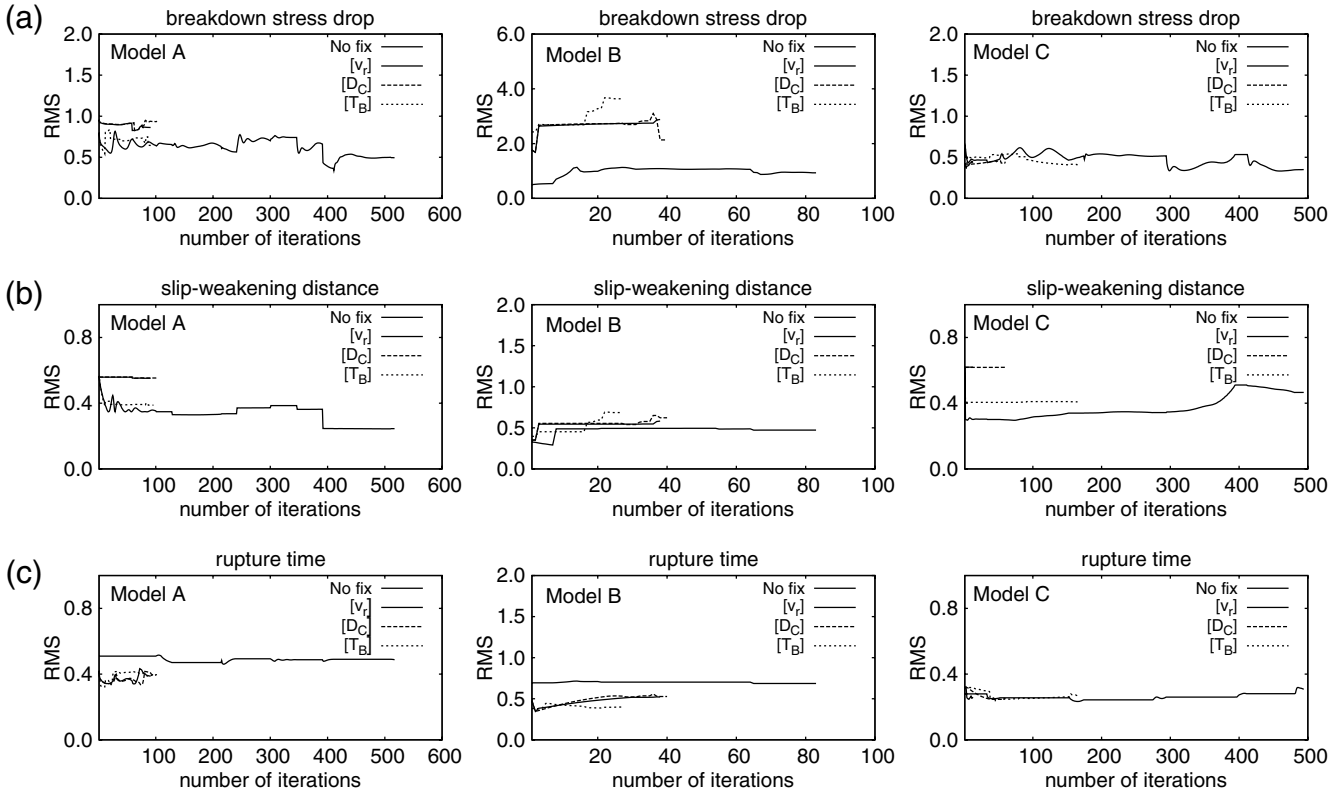

Figure 7. Convergence histories of (a) the breakdown stress drop, (b) the slip-weakening distance, and (c) the rupture time are represented by the rms value for Case-vr90 (model A on the left, model B in the center, and model C on the right).

parameter decreases, as shown in Figure 6. However, the estimated values are not guaranteed to be exact because the target value for the rupture velocity is not specified in most cases. An inadequate initial rupture velocity may cause the estimated results to a local minimum. Figure 8 shows the final J values (equation 19) normalized by the initial J value. All cases of parameter selection in the fixed stage are tested and their final J values are compared. For example, the comparison between no fix and $[v_r, T_B]$ shown on the left side in Figure 8 implies that when all parameters are allowed to be free, a poorer waveform fit is obtained than when v_r and T_B are fixed. It is not possible to obtain the converted solutions for all of the cases in our attempts considered here, but the cases including v_r in the fixed parameters yield small J values. Figure 7 shows the constant rms value of the rupture time resulting from the iterations. It implies that the other parameter in the trade-off pair, either the slip-weakening distance or the breakdown stress drop, may be varied in order to generate small J values.

The previously discussed results are consistent with the trade-off between the strength excess and the slip-weakening distance in the previous studies (Guatteri and Spudich, 2000) because the role of the strength excess is equivalent to that of the rupture time.

Figures 9 and 10 show the distributions of the estimated parameters and the estimated waveforms (0.0–1.2 Hz), respectively, for model A of the $[v_r]$ cases, namely, Case-vr50

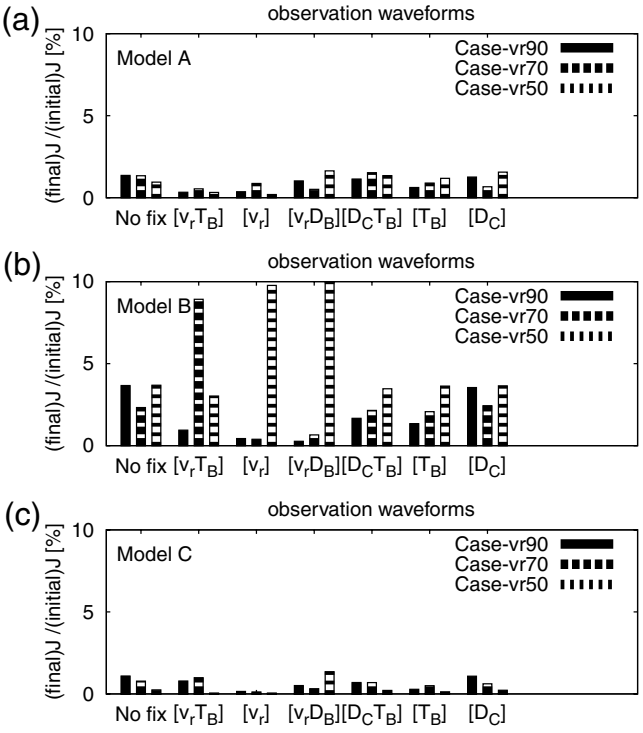

Figure 8. Final J values normalized by the initial J values for model A, model B, and model C.

and Case-vr90. Figures 9 and 10 also present the target distributions of the parameters and the target waveforms, respectively. The slip-weakening distance shown in Figure 9 is distributed with gradual changes around both of the fault edges because the slip-weakening distance is defined to be equal to the final slip displacement when the generated slip is shorter than the given slip-weakening distance. This is because we cannot uniquely identify the slip-weakening distance, and it can take an arbitrary value, even larger than the final slip displacement. Likewise, the stress drops are also treated. The region of the high breakdown stress drop is detected accurately for both cases, while its magnitude varies from half to twice the target values. In addition, the slip-weakening distance and the rupture time are underestimated by about half the target values. However, the difference

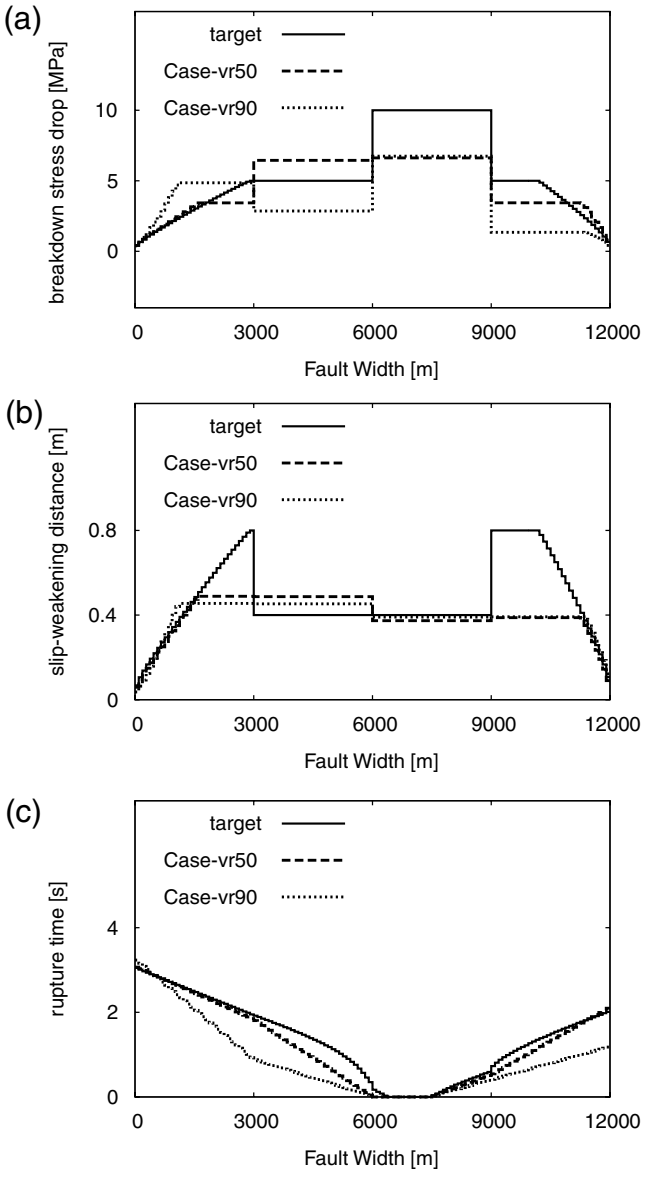

Figure 9. Distributions of estimated parameters and targets for model A of $[v_r]$ cases for Case-vr50 and Case-vr90.

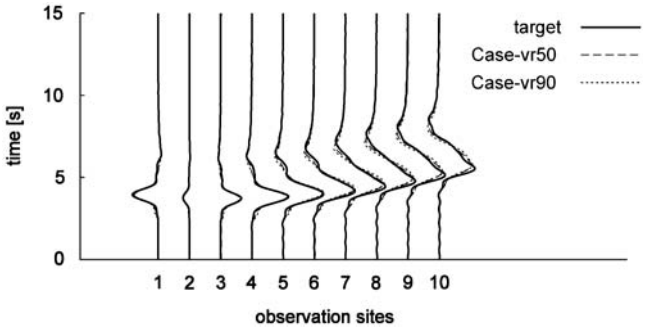

Figure 10. Estimated waveforms and targets for model A of $[v_r]$ cases for Case-vr50 and Case-vr90.

between the waveforms calculated from the estimated parameters and the target parameters is insignificant. Therefore, on the basis of the waveforms, it is impossible to tell which of the three models presented here is the best.

In order to understand the reasons for the previously discussed results, the time histories of the estimated slip rates are compared at three locations, namely, 2 km, 4 km, and 6 km from the top of the fault, as shown in Figure 11. The time that gives the peak slip rates for the two estimated results, called the peak time, corresponds well to the target, while the shapes between the rupture time and the peak time, called growing shapes, are different. The slip rates for the target grow rapidly, while those for Case-vr90 grow slowly. It is recognized that the difference in the growing shapes has a small effect on the synthetic waveforms, as shown in Figure 10.

We consider one of the simple examples, shown in Figure 12, in order to explain the relation between the trade-offs and the difference in growing shapes. In the example, we focus on a peak value of superposed slip rates because a waveform on a free surface originates from the superposition of slip rates with a time-shift due to the rupture velocity. In

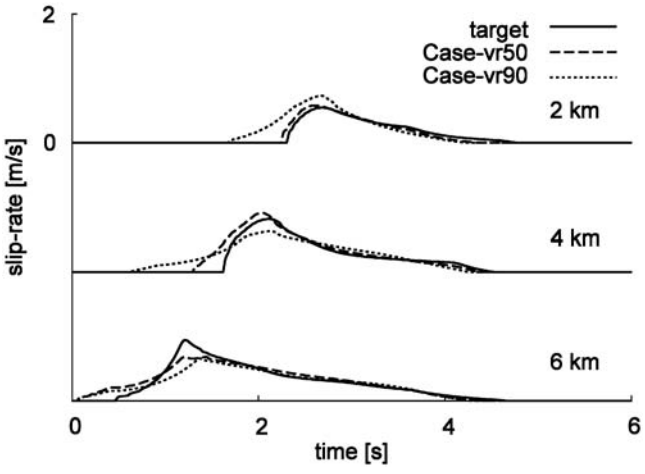

Figure 11. Comparison of the time histories of the estimated slip rate at 2 km, 4 km, and 6 km from the top of the fault. The growing shapes between the rupture time and the peak time are different.

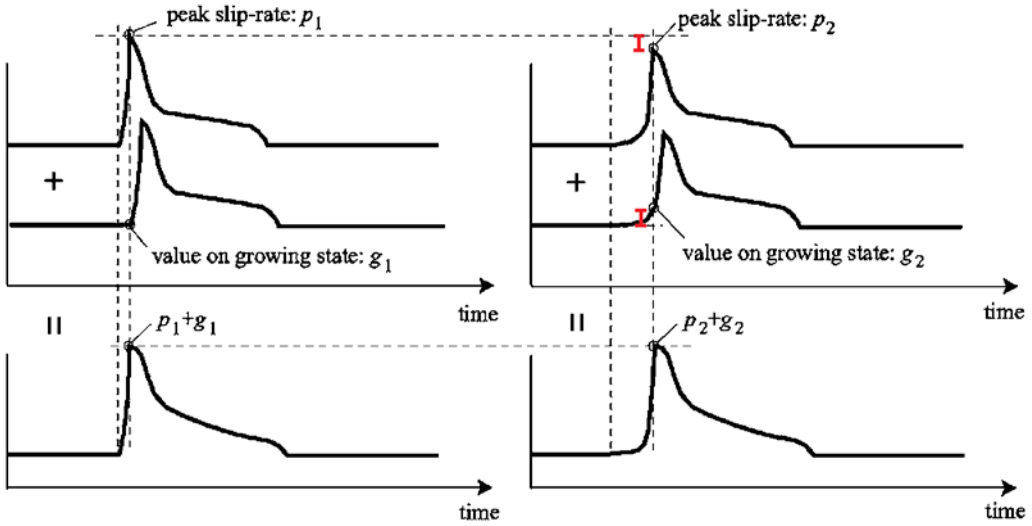

Figure 12. Schematic diagram illustrating the contribution of growing shapes to superposed slip rates. The color version of this figure is available only in the electronic edition.

Figure 12, rupture processes without and with significant growing shapes are shown on the left and right sides, respectively. If the peak values of the superposed slip rates are equal ($p_1 + g_1 = p_2 + g_2$), it is difficult to identify which process is correct. Because the value of the superposed slip rate for growing shapes is much smaller than the peak values, a small estimation error in the peak slip rate generates much variation in the rupture time. Therefore, the variation in the rupture times does not significantly contribute to the waveforms.

It is implied that the generation of different growing shapes with the same peak time is related to parameter trade-offs. Here, we focus on the analytical slip-rate time histories for a simple 1D assumption, namely, a constant slip rate over the entire fault plane (see Appendix A). When the slip displacement at the peak time t_p is equal to the slip-weakening distance, the following relation is derived among the parameters:

$$\frac{2\beta}{\mu}\frac{T_B}{D_C}\cdot(t_p - t_r) = -\log\left(\frac{T_S}{T_B + T_S}\right), \qquad (25)$$

where $T_S(\equiv\mu/2\beta\cdot\Delta\dot{u}_0)$ is an instantaneous stress drop just at the rupture time, where $\Delta\dot{u}_0$ is the initial slip rate at the rupture time t_r. T_B/D_C implies a gradient of the weakening curve. The argument of the logarithm on the right side depends on the instantaneous stress drop normalized by the breakdown stress drop. If the ratio is constant, T_B/D_C is related to $t_p - t_r$ with a -1 slope in the log–log plot.

In order to compare the previously discussed relation with the estimated results, the cases that were estimated well, whose final J values are less than 0.5% of the initial values, are selected from models A, B, and C. Figure 13 shows the relations between $t_p - t_r$ and T_B/D_C, normalized by each target value. From each inversion result, we can plot 128 points in Figure 13, because $t_p - t_r$ values vary inside the element of 93.75 m width. The size of the circular symbol shows the magnitude of the peak slip rate in order to emphasize that a small slip rate does not contribute to the waveforms. The distribution almost mirrors the -1 slope between the peak-to-rupture time, $t_p - t_r$, and the weakening gradient T_B/D_C.

$t_p - t_r$ and T_B/D_C comprise the trade-off pairs of the rupture parameter and the other parameter, as discussed in the previously introduced studies; the weakening gradient has not been addressed. Further, the slip-weakening

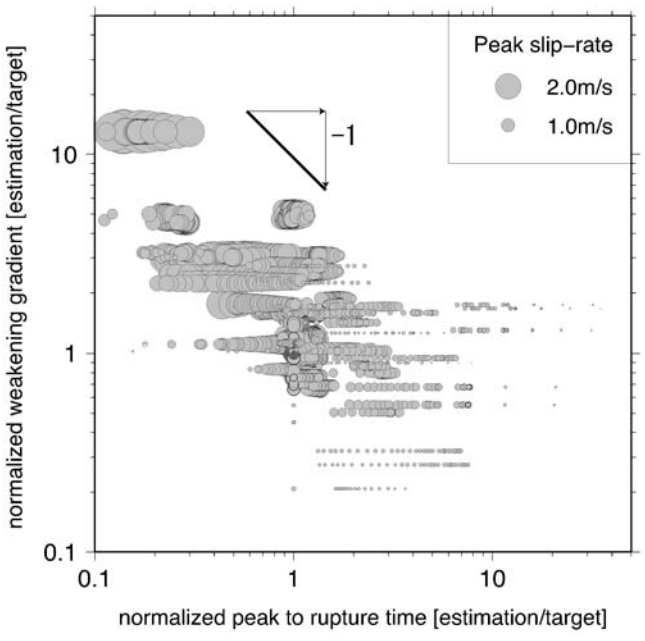

Figure 13. Relationship between the peak-to-rupture time and the weakening gradient, which is normalized by each target value. The size of the circular symbol shows the magnitude of the peak slip rate.

distance, which is longer than the generated slip displacement, cannot be detected according to its aforementioned definition.

For the same reason, the breakdown stress drop and the fracture energy cannot be detected if the generated slip does not exceed its own D_C and the generated breakdown stress drop does not exceed its own T_B. On the other hand, the weakening gradient is uniquely determined and is independent of the generated slip displacement. Then, the weakening gradient and the peak-to-rupture time should be selected for discussions on trade-offs because these parameters are uniquely determined.

Conclusions

We have applied dynamic source inversion to 2D synthetic tests in order to discuss parameter trade-offs. The results of the sensitivity tests, which consisted of numerous sets of inversions including a fixed stage and a released stage, imply trade-offs between the rupture parameter and the other parameters. It has been discovered from detailed comparisons of slip rates and waveforms that the growing shapes between the rupture time and the peak time do not contribute well to the generated waveforms. From a simple 1D assumption, the weakening gradient has been found to be analytically related to the peak-to-rupture time with a -1 slope in the log–log plot. In addition, the estimated values from the synthetic tests almost mirror the -1 slope.

For real earthquakes, the trade-offs may disturb the stable identification of the dynamic parameters. The values of the parameters should not be investigated from only bandlimited and noisy waveform data. In order to resolve this problem, it may be necessary to introduce some additional information obtained from small-scale experimental data, and/or to correct a number of estimated results in order to decrease the number of possible solution sets.

Data and Resources

No data were used in this article. Some plots were made using the Generic Mapping Tools version 4.3.1 (www.soest.hawaii.edu/gmt; Wessel and Smith, 1998).

Acknowledgments

We thank the two anonymous reviewers and editor David Douglas Oglesby for their thorough comments. We are grateful to the following persons for providing useful advice and discussions: Tomotaka Iwata, Takashi Miyatake, Kazuro Hirahara, Keiko Kuge, Jacobo Bielak, Luis A. Dalguer, and Nelson E. Pulido. We also extend our thanks to the many researchers who supplied us with important information. This article was supported in part by the Grant-in-Aid for Young Scientists Start-up of the Japan Society for the Promotion of Science.

References

Aagaard, B. T., G. Anderson, and K. W. Hudnut (2004). Dynamic rupture modeling of the transition from thrust to strike-slip motion in the 2002 Denali fault earthquake, Alaska, *Bull. Seismol. Soc. Am.* **94,** S190–S201.

Aochi, H., and E. Fukuyama (2002). Three-dimensional nonplanar simulation of the 1992 Landers earthquake, *J. Geophys. Res.* **107,** 2035.

Bouchon, M. (1997). The state of stress on some faults of the San Andreas system as inferred from near-field strong motion data, *J. Geophys. Res.* **102,** 11731–11744.

Cochard, A., and R. Madariaga (1994). Dynamic rupture faulting under rate-dependent friction, *Pure. Appl. Geophys.* **142,** 419–445.

Corish, S., C. Bradley, and K. Olsen (2007). Assessment of a nonlinear dynamic rupture inversion technique applied to a synthetic earthquake, *Bull. Seismol. Soc. Am.* **97,** 901–914.

Dalguer, L. A., K. Irikura, and J. Riera (2003). Generation of new cracks accompanied by the dynamic shear rupture propagation of the 2000 Tottori (Japan) earthquake, *Bull. Seismol. Soc. Am.* **93,** 2236–2252.

Dalguer, L. A., K. Irikura, W. Zhang, and J. D. Riera (2002). Distribution of dynamic and static stress changes during 2000 Tottori (Japan) earthquake: Brief interpretation of the earthquake sequences; foreshocks, mainshock and aftershocks, *Geophys. Res. Lett.* **29,** 1758.

Day, S. M., L. A. Dalguer, N. Lapusta, and Y. Liu (2005). Comparison of finite difference and boundary integral solutions to three-dimensional spontaneous rupture, *J. Geophys. Res.* **110,** B12307.

Fukuyama, E., and T. Mikumo (2006). Dynamic rupture propagation during the 1891 Nobi, central Japan, earthquake: A possible extension to the branched faults, *Bull. Seismol. Soc. Am.* **96,** 1257–1266.

Goto, H., and S. Sawada (2006a). Dynamic source inversion based on stable formulation and on identification of the resolution level via a multiscale approach, *Geophys. J. Int.* **167,** 779–793.

Goto, H., and S. Sawada (2006b). Dynamic source inversion based on stable formulation, *Proc. of the 1st Eur. Conf. Earthq. Eng. Seismol.*, no. 1539, 1–10.

Goto, H., L. Ramirez-Guzman, and J. Bielak (2008). Numerical simulation of dynamic fault rupture propagation based on a combination of BIEM and FEM solutions, *Proc. of the 14th World Conf. Earthq. Eng.*, 12–17 October 2008, Beijuing, China.

Guatteri, M., and P. Spudich (2000). What can strong-motion data tell us about slip-weakening fault-friction laws?, *Bull. Seismol. Soc. Am.* **90,** 98–116.

Harris, R. A., J. F. Dolan, R. Hartleb, and S. M. Day (2002). The 1999 Izmit, Turkey, earthquake: A 3D dynamic stress transfer model of intraearthquake triggering, *Bull. Seismol. Soc. Am.* **92,** 245–255.

Ida, Y. (1972). Cohesive force across the tip of a longitudinal-shear crack and Griffith's specific surface energy, *J. Geophys. Res.* **77,** 3796–3805.

Ide, S., and M. Takeo (1997). Determination of constitutive relations of fault slip based on seismic wave analysis, *J. Geophys. Res.* **102,** 27379–27391.

Mikumo, T., K. B. Olsen, E. Fukuyama, and Y. Yagi (2003). Stress-breakdown time and slip-weakening distance inferred from slip-velocity functions on earthquake faults, *Bull. Seismol. Soc. Am.* **93,** 264–282.

Miyatake, T. (1992a). Reconstruction of dynamic rupture process of an earthquake with constraints of kinematic parameters, *Geophys. Res. Lett.* **19,** 349–352.

Miyatake, T. (1992b). Dynamic rupture process of inland earthquakes in Japan weak and strong asperities, *Geophys. Res. Lett.* **19,** 1041–1044.

Miyatake, T., Y. Yagi, and T. Yasuda (2004). The dynamic rupture process of the 2001 Geiyo, Japan, earthquake, *Geophys. Res. Lett.* **31,** L12612.

Ohnaka, M. (2003). A constitutive scaling law and a unified comprehension for frictional slip failure, shear fracture of intact rock, and earthquake rupture, *J. Geophys. Res.* **108,** 2080.

Peyrat, S., and K. Olsen (2004). Nonlinear dynamic rupture inversion of 2000 western Tottori Japan, earthquake, *Geophys. Res. Lett.* **31,** L05604.

Peyrat, S., K. Olsen, and R. Madariaga (2004). Which dynamic rupture parameters can be estimated from strong ground motion and geodetic data?, *Pure Appl. Geophys.* **161,** 2155–2169.

Pulido, N., and K. Irikura (2000). Estimation of dynamic rupture parameters from the radiated seismic energy and apparent stress, *Geophys. Res. Lett.* **27,** 3945–3948.

Quin, H. (1990). Dynamic stress drop and rupture dynamics of the October 15, 1979 Imperial Valley, California earthquake, *Tectonophysics* **175,** 93–117.

Song, S. G., and G. C. Beroza (2004). A simple dynamic model for the 1995 Kobe, Japan earthquake, *Geophys. Res. Lett.* **31,** L18613.

Walsh, J. L. (1923). A closed set of normal orthogonal functions, *American J. Mathematics* **45,** 5–24.

Wessel, P., and W. H. F. Smith (1998). New, improved version of generic mapping tools released, *Eos Trans. AGU* **79,** 579.

Zhang, W., T. Iwata, K. Irikura, A. Pitarka, and H. Sekiguchi (2004). Dynamic rupture process of the 1999 Chi-Chi, Taiwan, earthquake, *Geophys. Res. Lett.* **31,** L10695.

Appendix A

As a hypothetical situation, we assume space distributions of slip rates to be constant. This is called a 1D assumption. From equation (3), the BIE in the 1D assumption is written as the following simple formulation by reducing the space integration:

$$T(t) = T_I - \frac{\mu}{2\beta}\Delta\dot{u}_3(t). \tag{A1}$$

The system of equations, which consists of the friction law (equations 1 and 2) and the BIE (equation A1), can then be solved analytically. The time history for the slip rate is the solution of the following first-order differential equations:

$$\begin{aligned} &\Delta u_3(t) = 0 \quad \text{for } t < t_r \\ &\frac{\mu}{2\beta}\Delta\dot{u}_3(t) - \frac{T_B}{D_C}\Delta u_3(t) = T_S \quad \text{for } t_r \le t \le t_p \\ &\frac{\mu}{2\beta}\Delta\dot{u}_3(t) = T_B + T_S \quad \text{for } t_p < t, \end{aligned} \tag{A2}$$

where $T_S = \mu/2\beta \cdot \Delta\dot{u}_0$, which implies an instantaneous stress drop precisely at the rupture time, and $\Delta\dot{u}_0$ represent an instantaneous slip rate applied precisely at the rupture time t_r.

The initial conditions are defined for each equation in equation (A2) as follows:

$$\begin{aligned} &\Delta u_3 = 0 \quad \text{at } t = 0 \qquad \Delta u_3 = 0 \quad \text{at } t = t_r \\ &\Delta u_3 = D_C \quad \text{at } t = t_p. \end{aligned} \tag{A3}$$

The analytical solutions for equations (A2) and (A3) are as follows:

$$\begin{aligned} &\Delta u_3(t) = 0 \quad \text{for } t < t_r \\ &\Delta u_3(t) = \frac{D_C T_S}{T_B}\left\{\exp\left[\frac{2\beta}{\mu}\frac{T_B}{D_C}\cdot(t - t_r)\right] - 1\right\} \\ &\qquad \text{for } t_r \le t \le t_p \\ &\Delta u_3(t) = \frac{2\beta}{\mu}(T_B + T_S)\cdot(t - t_p) + D_C \\ &\qquad \text{for } t_p < t. \end{aligned} \tag{A4}$$

In the 1D assumption, the slip rate for $t \to \infty$ is still finite. The reason is that the overestimation of a distant region on the fault plane is overestimated due to a reduction in the space integration from the original BIE in equation (3). However, the effect of the overestimation is expected to be less around the rupture time than $t \to \infty$ because the influence of distant regions is limited.

From the second equation in equation (A4), the following relation is required in order to satisfy $\Delta u_3(t_p) = D_C$:

$$\frac{2\beta}{\mu}\frac{T_B}{D_C}\cdot(t_p - t_r) = -\log\left(\frac{T_S}{T_B + T_S}\right). \tag{A5}$$

Disaster Prevention Research Institute
Kyoto University
Gokasho, Uji
Kyoto, 611-0011, Japan

Manuscript received 24 August 2008